JOURNAL OF SPACECRAFT AND ROCKETS
Vol. 37, No. 2, March–April 2000

Simulations of Shock-Wave Reflections in Nonequilibrium Flows

F. Grasso* and R. Paoli†
University of Rome "La Sapienza," 00184 Rome, Italy

Thermochemical nonequilibrium effects on shock-wave reflection phenomena in two-dimensional steady flows are studied. The physical model is based on a two-temperature model for the vibrational relaxation and the reduced Park's model for nonequilibrium chemistry. The computational strategy relies on a patched subdomain decomposition that exploits massively parallel architectures and uses a finite volume second-order upwind-biased total variation diminishing scheme as the basic numerical algorithm. Several simulations have been performed to characterize the scales of Mach reflection configurations and to detect the hysteresis in the presence of vibrational and chemical relaxation.

Introduction

IN the present paper real gas effects on shock-wave reflections in two-dimensional steady flows are studied. These phenomena play an important role in most aerospace applications, such as, for example, supersonic intakes, wind-tunnel design, and complex configurations characterized by shock-shock interactions (Edney type III-II). Two shock-wave reflection configurations are possible in steady flows, namely regular reflection (RR) and Mach reflection (MR). The RR consists of two shock waves: the incident i and reflected r ones, which meet at the reflection point R of either a reflecting surface or, equivalently, a symmetry plane. A qualitative sketch of the MR pattern for a double-wedge configuration is shown in Fig. 1. The MR consists of three shock waves: the incident i, the reflected r, and the Mach stem m, which is nearly straight and normal to the reflecting surface. The flow is supersonic in regions 1 and 2 and is subsonic in region 3, and a slip line s separates states 2 and 3.

The interaction of the expansion fan f generated at the trailing edge of the wedge with the slip line causes the pressure to drop in the streamwise direction, thus accelerating the flow that eventually attains supersonic conditions again. As a consequence, the area of the stream tube between the two slip lines emanating at the two triple points M first decreases to a minimum and then increases in the region where the flow becomes supersonic. Therefore, an MR is characterized by the presence of a subsonic pocket in a supersonic flow whose size (i.e., the distance between the Mach stem location and the position where the flow attains sonic conditions) depends solely on the wedge geometry,[1] provided nonequilibrium effects are negligible. However, in the presence of nonequilibrium, the MR pattern depends not only on the geometric scales but also on the thermal and/or chemical relaxation lengths.[2–4]

In the past two decades several experimental, theoretical, and numerical papers on shock-wave reflections in steady flows have been published. For ideal gases a semianalytical model[1] has been developed to estimate the scales of an MR configuration by solving the integral form of the continuity and momentum equations together with the three-shock theory of von Neumann. Hornung et al.[2] have experimentally studied the influence of the shock strength on shock-wave reflections and have shown the occurrence of the transition from RR to MR. In addition, they have ascertained that, for a given Mach number, there is a range of shock angles that are bounded by the von Neumann α_N and the detachment α_d limits where both reflections are admissible [i.e., the existence of a dual solution region (DS)]. In the absence of nonequilibrium phenomena, the detachment and von Neumann angles depend on the thermodynamic properties of the gas through the specific heat ratio γ, and can be determined by means of the three-shock theory of von Neumann.

For cold high-speed flows, experimental[2,5] and numerical[6,7] investigations indeed indicate that the transition between RR and MR obeys a hysteresis mechanism: if the shock angle is increased (starting from values below α_N), a regular reflection always occurs, and it is maintained throughout the DS region up to the detachment limit, where it suddenly changes to an MR. However, if the shock angle is reduced starting from values above α_d, an MR is always established in the DS region up to the von Neumann angle. Hence, the shock reflection in the DS region depends on the flow history; the accepted transition criteria are the von Neumann (equilibrium) criterion for MR→RR transition occurring at α_N and detachment criterion for RR→MR transition occurring at α_d. The latter has been confirmed through numerical simulations by Ivanov et al.[8] who used both an inviscid continuum (Euler) and kinetic [direct simulation Monte Carlo method (DSMC)] approach. However, as noted in Refs. 7 and 9, RR→MR transitions can be affected by the three-dimensionality of the flow as well as the viscous growth of the shear layer downstream of the triple point. Indeed, Hornung and Robinson[9] could not observe any hysteresis phenomenon; likewise, Chpoun et al.[5] observed a RR→MR transition at an angle less than α_d.

To the authors' knowledge very few papers dealing with the influence of thermal and chemical relaxation on the shock reflection and hysteresis have been published. A first-order estimate of the real gas effects on RR⇔MR transitions can be obtained by assuming different specific heat ratios. References 4 and 10 indicate that, in the case of high freestream temperature, the incident shock can be assumed as frozen while the region downstream of the reflected shock exhibits thermal equilibrium. Therefore, an estimation of the dependency of α_N and α_d upon the Mach number can be obtained by considering two values of γ (1.4 and 1.29 corresponding, respectively, to frozen conditions and fully vibrational excitation). The distributions of α_N and α_d as a function of the freestream Mach number are reported in Fig. 2, which shows that the reduction of γ leads to 1) an enlargment of the DS region (i.e., the hysteresis phenomenon is more important), and 2) the detachment criterion is most affected by real gas effects, whereas the equilibrium criterion is affected the least.

Hornung et al.[2] suggest that, in the presence of nonequilibrium, the relaxation length ℓ affects the transition to MR, provided ℓ is comparable to the length scale of the problem. Hornung et al.[2] have experimentally studied the influence of molecular vibration and dissociation and obtained a reduction and a forward displacement of the Mach stem, as well as an increase of the detachment angle, thus proving the influence of relaxation phenomena on the RR→MR transition. Burtschell and Zeitoun[11] have analyzed the effects of thermochemical relaxation processes and have observed an increase in the detachment angle and the reduction of the Mach stem height; in addition, they have also shown that such a reduction is affected by vibration-dissociation coupling. Gimelshein et al.[3,10] have

Received 6 July 1999; revision received 3 December 1999; accepted for publication 6 December 1999.

*Associate Professor, Department of Mechanics and Aeronautics, Via Eudossiana, 18. Associate Fellow AIAA.

†Ph.D. Student, Department of Mechanics and Aeronautics, Via Eudossiana, 18.

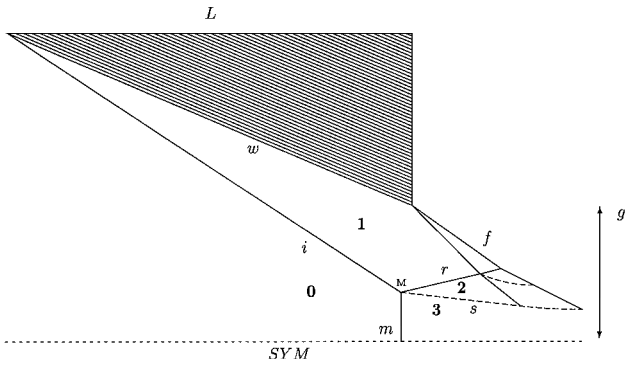

Fig. 1 Sketch of an MR configuration.

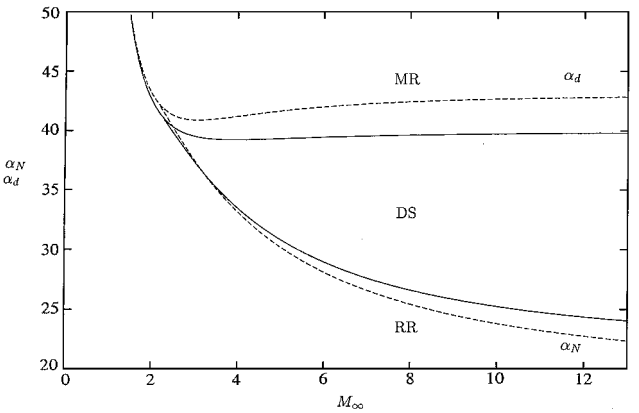

Fig. 2 Distribution of von Neumann α_N and detachment α_d angles as a function of freestream Mach number: ——, $\gamma = 1.4$, and – – –, $\gamma = 1.29$.

numerically observed the effects of relaxation and high Knudsen numbers on shock-wave reflection in a nitrogen gas by means of a DSMC and confirmed the occurrence of the hysteresis with a delay in the RR→MR transition. As pointed out in Ref. 10, studies on MR→RR transition are rather difficult on account of the fact that when α approaches α_N an MR occurs in the limit of vanishing Mach stem height, thus making it difficult to resolve.

At high Mach numbers, in the presence of relaxation phenomena, the theoretical estimation of the scales of the MR reflection requires a detailed analysis of the flow evolution within the subsonic pocket.[4] The present authors have recently developed a semianalytical approach that solves the quasi-one-dimensional equations in the subsonic pocket and have estimated the effects of thermal and chemical relaxation on the Mach stem height and its position and on the size of the pocket.[4] The results confirm the reduction of the scales of the MR configuration and its forward displacement in the presence of nonequilibrium phenomena.

The objective of the present work is to assess the influence of thermal and chemical relaxation on shock reflection and hysteresis by using a continuum approach based on the solution of the conservation laws that account for vibrational relaxation, finite rate chemistry, and molecular transport. In the following sections the model equations are derived, and the numerical approach that exploits a subdomain decomposition for parallel applications is described. Numerical simulations at two flow conditions (corresponding to flight and wind-tunnel conditions) are presented and compared with cold flow simulations that have also been carried out in order to quantify the effects of thermal and chemical nonequilibrium. For the cold flow simulations we have assumed different specific heat ratios for the two test conditions. The scales of the shock reflection configuration are also compared with those predicted by semianalytical models,[1,4] as well as with results (either numerical or experimental) available in the literature.

Governing Equations

The model accounts for thermal and chemical nonequilibrium, and it is based on a two-temperature model that assumes a single vibrational temperature T_V to characterize the vibrational relaxation of diatomic species. In vector form the conservation equations for a multispecies nonionizing gas are

$$\frac{\partial}{\partial t}\int_V \boldsymbol{w}\,\mathrm{d}V + \oint_{\partial V} \boldsymbol{f}\cdot\boldsymbol{n}\,\mathrm{d}S = \int_V \dot{\boldsymbol{w}}\,\mathrm{d}V \tag{1}$$

where

$$\begin{aligned}
\boldsymbol{w} &= [\rho_s, \rho u, \rho v, \rho E, \rho e_V]^T, \qquad \boldsymbol{f} = \boldsymbol{f}_E - \boldsymbol{f}_V \\
\boldsymbol{f}_E &= [\rho_s \boldsymbol{u}, \rho \boldsymbol{u}\otimes\boldsymbol{u} + p\boldsymbol{I}, \rho \boldsymbol{u} H, \rho \boldsymbol{u} e_V]^T \\
\boldsymbol{f}_V &= [-\rho_s \boldsymbol{V}_s, \boldsymbol{\sigma}, \boldsymbol{\sigma}\cdot\boldsymbol{u} - \boldsymbol{q}, -\boldsymbol{q}_V]^T \\
\dot{\boldsymbol{w}} &= [\dot{\rho}_s, 0, 0, 0, S_{T-V} + S_{V-D}]^T \qquad (2) \\
\boldsymbol{\sigma} &= \mu(\nabla\boldsymbol{u} + \nabla\boldsymbol{u}^T) - \tfrac{2}{3}\mu\nabla\cdot\boldsymbol{u}\boldsymbol{I} \\
\boldsymbol{q} &= -\eta_{\mathrm{tr}}\nabla T - \eta_V \nabla T_V - \sum_s \rho h_s D_s \nabla X_s \\
\boldsymbol{q}_V &= -\eta_V \nabla T_V - \sum_s \rho h_{s,V} D_s \nabla X_s
\end{aligned}$$

$$H = E + \frac{p}{\rho} = \sum_s Y_s e_s + \frac{u^2+v^2}{2} + \frac{p}{\rho}, \qquad p = \sum_s \rho_s R_s T \tag{3}$$

with $\boldsymbol{\sigma}, \boldsymbol{q}, \boldsymbol{q}_V, H, h_{s,V}$, and e_s, respectively, the stress tensor, the energy diffusion flux (caused by translational-rotational and vibrational energy conduction and species diffusion), the vibrational energy diffusion (caused by vibrational energy conduction and diffusion of diatomic species), the total enthalpy, the vibrational enthalpy, and internal energy of species.

For atomic species e_s accounts only for the translational energy contribution:

$$e_s = e_{s,T} + \Delta h_s^0 = \tfrac{3}{2} R_s T + \Delta h_s^0 \tag{4}$$

whereas for diatomic species e_s also accounts for rotation and vibration and

$$e_s = e_{s,T} + e_{s,V} + \Delta h_s^0 = \frac{5}{2} R_s T + \frac{R_s \theta_{s,v}}{\exp(\theta_{s,v}/T_V) - 1} + \Delta h_s^0 \tag{5}$$

where $\theta_{s,v}$ and Δh_s^0 are, respectively, the characteristic vibrational temperature and the enthalpy of formation. With regard to the transport coefficients (μ, η_{tr}, η_V, and D_s), they are defined according to the Chapmann–Enskog theory.[12,13] In the present paper we have carried out simulations both for diatomic nitrogen and for air, and the finite rate chemistry has been modeled by means of Park's reaction mechanism.[14] To account for the coupling between vibration and dissociation, we have introduced a rate-controlling temperature for the dissociation reactions defined as $T_d = \sqrt{(T T_V)}$. The vibrational source terms represent, respectively, the translational–vibrational energy exchange (S_{T-V}) and the energy removal contribution caused by vibration-dissociation coupling (S_{V-D}), and they have been modeled as discussed in Ref. 13.

Numerics

The numerical simulations of high-speed flows in nonequilibrium require the use of robust and accurate schemes and are computationally intensive. In the present work we have devised a computational strategy based on a patched subdomain decomposition[15] that exploits parallel computers, whereby the solution on all domains is obtained concurrently by reducing the very large-scale problem to several small-scale partitions of the same problem. In general, there are two alternatives for subdividing the computational domain: the first one introduces domains that can overlay and can have an arbitrary orientation[15]; the second one subdivides the computational domain into patched zones that share common boundaries (interfaces) without overlapping. The main advantage of the overlaid subdomain decomposition is the flexibility in grid generation; however,

difficulties may arise in ensuring conservation, and, moreover, the effects of the size of overlaid zones on the accuracy and convergence rate are difficult to predict. Patched subdomain decomposition introduces some constraints on the grid generation. However, it makes it simple to ensure 1) a conservative interface treatment and 2) no distortion of discontinuities (such as shocks and slip surfaces) that cross interfaces.

The basic numerical algorithm is based on a cell-centered finite volume patched subdomain formulation, and the governing equations are cast in the following fully discretized form:

$$V_{i,j}\frac{\mathrm{d}\boldsymbol{w}_{i,j}}{\mathrm{d}t}+\sum_{\beta=1}^{4}(\boldsymbol{f}_{E,\mathrm{num}}-\boldsymbol{f}_{V,\mathrm{num}})_{\beta}\cdot\boldsymbol{n}_{\beta}\Delta s_{\beta}=V_{i,j}\dot{\boldsymbol{w}}_{i,j} \tag{6}$$

where $V_{i,j}$ and Δs_β are, respectively, the cell volume and the surface area of face β, and $\boldsymbol{f}_{E,\mathrm{num}}$ and $\boldsymbol{f}_{V,\mathrm{num}}$ represent, respectively, the numerical inviscid and viscous flux functions.

The numerical approximation of the inviscid flux is based on a secord-order upwind-biased total variation diminishing scheme that accounts for nonequilibrium phenomena, following the general methodology described in Refs. 13 and 16. For example, the numerical inviscid flux discretization at the generic cell face $(i+\frac{1}{2}, j)$ is cast in the following form:

$$(\boldsymbol{f}_{E,\mathrm{num}}\cdot\boldsymbol{n})_{i+\frac{1}{2},j}=\frac{1}{2}\left[(\boldsymbol{f}_{E}\cdot\boldsymbol{n})_{i,j}+(\boldsymbol{f}_{E}\cdot\boldsymbol{n})_{i+1,j}+\boldsymbol{R}_{i+\frac{1}{2},j}\boldsymbol{\Phi}_{i+\frac{1}{2},j}\right] \tag{7}$$

The expression for the elements (ϕ^ℓ) of the vector $\boldsymbol{\Phi}$ is obtained by characteristic decomposition in the direction normal to the cell face and the use of a minmod slope limiter:

$$\phi^{\ell}_{i+\frac{1}{2},j}=\tfrac{1}{2}\psi\left(a^{\ell}_{i+\frac{1}{2},j}\right)\left(g^{\ell}_{i+\frac{1}{2},j}+g^{\ell}_{i,j}\right)-\psi\left(a^{\ell}_{i+\frac{1}{2},j}+\gamma^{\ell}_{i+\frac{1}{2},j}\right)\alpha^{\ell}_{i+\frac{1}{2},j} \tag{8}$$

where

$$\alpha_{i+\frac{1}{2},j}=\boldsymbol{R}^{-1}_{i+\frac{1}{2},j}\left(\boldsymbol{w}_{i+\frac{1}{2},j}-\boldsymbol{w}_{i,j}\right)$$

$$\gamma^{\ell}_{i+\frac{1}{2},j}=\frac{\frac{1}{2}\psi\left(a_{i+\frac{1}{2},j}\right)\left(g^{\ell}_{i+\frac{1}{2},j}-g^{l}_{i,j}\right)}{\alpha^{\ell}_{i+\frac{1}{2},j}}$$

$$g^{\ell}_{i,j}=\mathrm{minmod}\left(\alpha^{\ell}_{i+\frac{1}{2},j},\alpha^{\ell}_{i-\frac{1}{2},j}\right)$$

$$\mathrm{minmod}(x,y)=\mathrm{sign}(x)\max\{0,\min[|x|,y\,\mathrm{sign}(x)]\} \tag{9}$$

and $\psi(z)$ is Harten's entropy correction to $|z|$.[13] The right eigenvector matrix is defined as

$$\boldsymbol{R}=\begin{bmatrix}\delta_{\mathrm{sq}} & 0 & Y_s & Y_s & Y_s\\ u & -cn_y & 0 & u+cn_x & u-cn_x\\ v & cn_x & 0 & v+cn_x & v-cn_y\\ \boldsymbol{u}\cdot\boldsymbol{u}/2-\chi_q/K & c(\boldsymbol{u}\cdot\boldsymbol{b}) & 1 & H+cn_x & H-cn_y\\ 0 & 0 & 1 & e_V & e_V\end{bmatrix} \tag{10}$$

where $\boldsymbol{b}\cdot\boldsymbol{n}=0$ and the pressure derivatives K and χ_q are defined as

$$K=\frac{\sum_s Y_s R_s}{\sum_s Y_s c_{v_{s,T}}},\qquad \chi_q=R_q T-Ke_{q,T}$$

and Y_s, $c_{v_{s,T}}$ and c^2 are, respectively, the mass fraction, the species translational-rotational specific heat, and the frozen speed of sound that are defined as

$$Y_s=\frac{\rho_s}{\rho},\qquad c_{v_{s,T}}=\frac{\partial e_{s,T}}{\partial T},\qquad c^2=\sum_q \chi_q Y_q+K(h-e_V)$$

and

$$h=\sum_s Y_s e_s+p/\rho$$

The values at cell interfaces are calculated by using a generalization of Roe's averaging[17] to allow for thermal and chemical nonequilibrium.

The numerical viscous fluxes are evaluated by using a second-order central discretization. In the presence of nonequilibrium flows, stiffness arises for the disparity between the characteristic timescale of the relaxation processes and the fluid dynamic one. For steady flows stiffness can be reduced by preconditioning the system of discretized ordinary differential equations. The time integration is then performed by a three-stage Runge–Kutta algorithm where the source terms are treated by a point implicit algorithm,[13] by introducing a precondition matrix that is related to the partial Jacobian of the source term.

All computations have been carried out by partitioning the computational domain in 32 subdomains as a compromise for speed up and load balancing. The partitioning of the computational domain introduces interfaces between adjacent zones. Therefore, the use of a subdomain technique requires boundary conditions not only along the true physical boundaries but also at the interfaces.[15] In the present work we have enforced the continuity of the variables along the boundaries shared by two adjacent subdomains. However, for an efficient treatment of the boundary conditions (and to maintain a second-order accuracy), we have introduced two fictitious layers of cells, thus making the patched subdomains effectively overlaid. Then, the interface conditions are enforced by injecting the solution of the underlying subdomain onto the overlaying one.

Results

Several simulations of shock-wave reflections for a double-wedge configuration of given size $g/w=0.4$ (see Fig. 1) have been carried out with the objective of determining the influence of thermal and chemical relaxation phenomena on 1) the flow structure, 2) the scales of the Mach stem configuration, and 3) the hysteresis. Two flow conditions have been considered corresponding to flight- and wind-tunnel-type conditions. The former corresponds to air at $u_\infty=2400$ m/s, $p_\infty=20.35$ Pa, $T_\infty=252$ K (for an altitude of 60 km and $M_\infty=7.5$), and the wedge size is $w=1$ m. The other flow condition refers to diatomic nitrogen at $u_\infty=7060$ m/s, $p_\infty=723$ Pa, $T_\infty=1100$ K (wind-tunnel conditions at $M_\infty=9.8$) with $w=4$ cm. For the purpose of assessing the influence of real gas effects, we have also performed ideal gas simulations for the same flow conditions.

All computations have been carried out on a mesh M1 consisting of 24,200 total number of cells whose value has been selected through a (limited) grid sensitivity study of MR at flight-type conditions. The influence of the total number of mesh points N_t was analyzed by considering two additional grids M2 and M3 with, re-

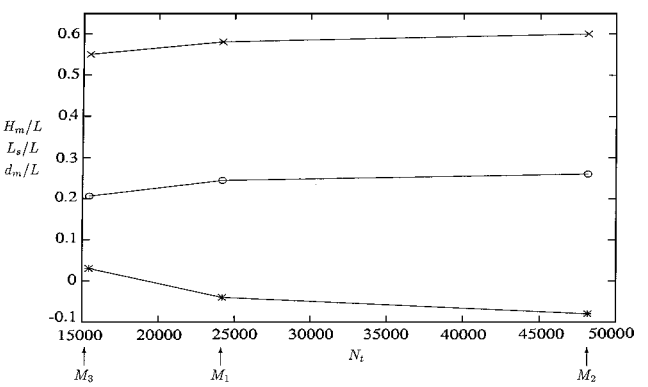

Fig. 3 Grid sensitivity analysis. Influence of total number of cells on MR scales ($M_\infty=7.5$ and $\theta_w=30.5$ deg): ○, Mach stem height H_m/L; ∗, Mach stem position d_m/L; and ×, length of the subsonic pocket L_s/L.

spectively, 48,150 and 15,450 total number of cells. The computed values of the Mach stem scales for the case of an MR configuration at $\theta_w = 30.5$ are shown in Fig. 3, where the Mach stem height H_m, the extent of the subsonic pocket L_s, and the location of the Mach stem d_m (measured with respect to the trailing edge of the wedge, i.e., $d_m = x_m - L$) are reported as a function of N_t. In particular, the figure shows that the percentage differences in the predicted Mach stem height of the finer (M2) and the coarser (M3) grids with respect to M1, are, respectively, of $\mathcal{O}(5\%)$ and $\mathcal{O}(15\%)$. Consequently, for all computations grid M1 was selected as a good compromise for accuracy, grid independence, and computational costs. A graphical example of the selected computational grids is reported in Fig. 4 for the case $M = 7.5$ and $\theta_w = 30.5$ deg.

With regard to the boundary conditions (Fig. 5), we have imposed 1) uniform conditions along the inflow boundary, 2) symmetry along the bottom and upper boundaries, 3) non-slip noncatalytic wall conditions and given wall temperature ($T_w = 300$ K), and 4) extrapolation conditions at the outflow. To inhibit the upstream influence of the outflow boundary treatment, we have selected a computational domain that extends for three wedge sizes in the rear region. All quantities have been nondimensionalized as follows: pressure and temperature by their freestream values (p_∞, T_∞), species partial densities by freestream total density (ρ_∞), and velocities and energies, respectively, by $\sqrt{(p_\infty/\rho_\infty)}$ and p_∞/ρ_∞.

To determine the influence of nonequilibrium phenomena on the hysteresis, for all cases the flowfield is initialized in the DS region assuming uniform conditions, thus initially obtaining a RR. Once a stationary solution is obtained, the wedge is rotated around the trailing edge so as to generate a shock wave with a different shock angle. When stationary conditions are achieved, the wedge is rotated again; this process is repeated so as to cover an hysteresis loop DS→ MR→ DS (for space limitations we only discuss results corresponding to one wedge angle). To quantify the effects of the thermal nonequilibrium, we have also carried out cold flow simulations assuming different specific heat ratio for the two test conditions.

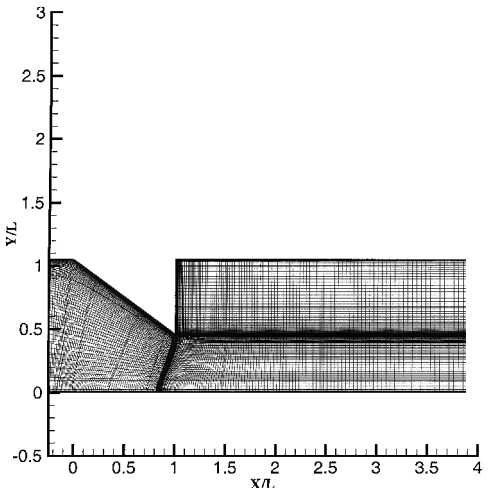

Fig. 4 Example of selected computational grid (with 32 blocks) for the case $M_\infty = 7.5$ and $\theta_w = 30.5i$ deg.

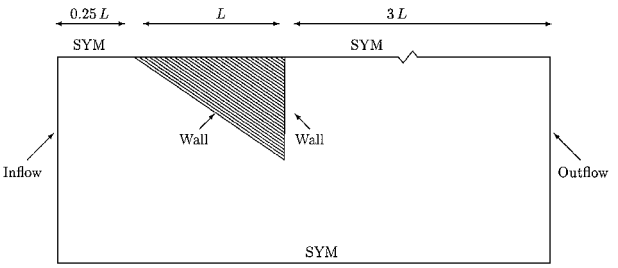

Fig. 5 Computational domain and boundary conditions.

Flight Conditions

The extrema of the hysteresis loop correspond to variations of the wedge angle in the range 30.5 deg $< \theta_w <$ 31.5 deg. The iso-density distributions for the bottom and upper conditions of the loop are reported in Fig. 6, which clearly shows the occurrence of the hysteresis. Mach reflections exhibit a structure that consists of a thermally and chemically frozen three-shock configuration with a relaxation occurring behind the Mach stem in the subsonic pocket. The results also show that the expansion waves generated at the trailing edge of the shock remain nearly straight, as argued in Refs. 1 and 4. The translational and vibrational iso-temperature distributions reported in Fig. 7 show that, because of the expansion in the pocket, translation and vibration do not attain equilibrium. This is also confirmed by the distributions of the translational and vibrational temperatures

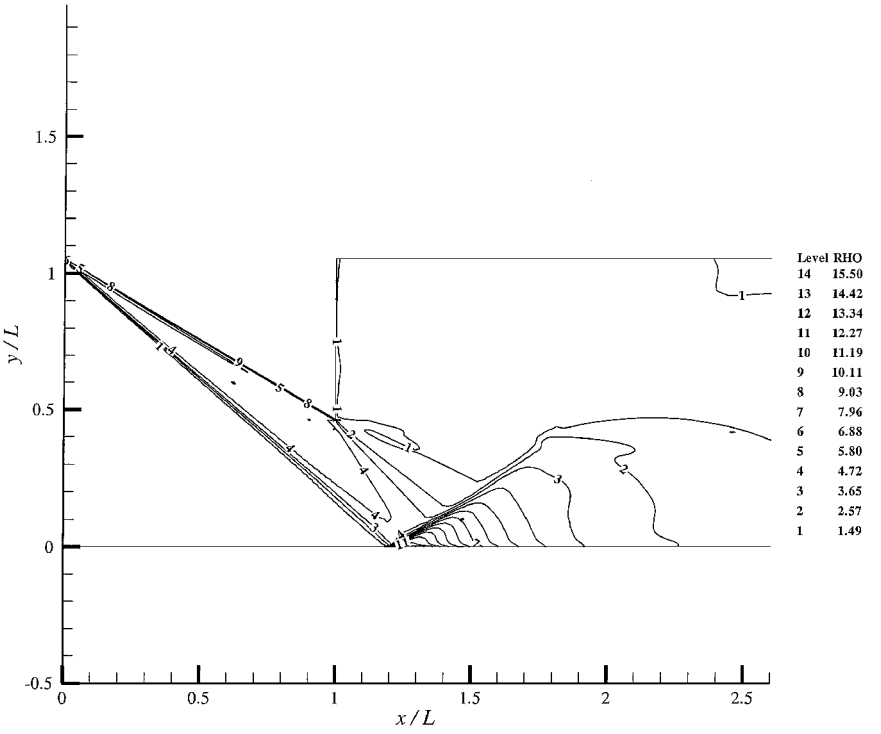

Regular reflection, $\theta_w = 30.5$ deg

Fig. 6 Hysteresis loop at $M_\infty = 7.5$: iso-density contour lines.

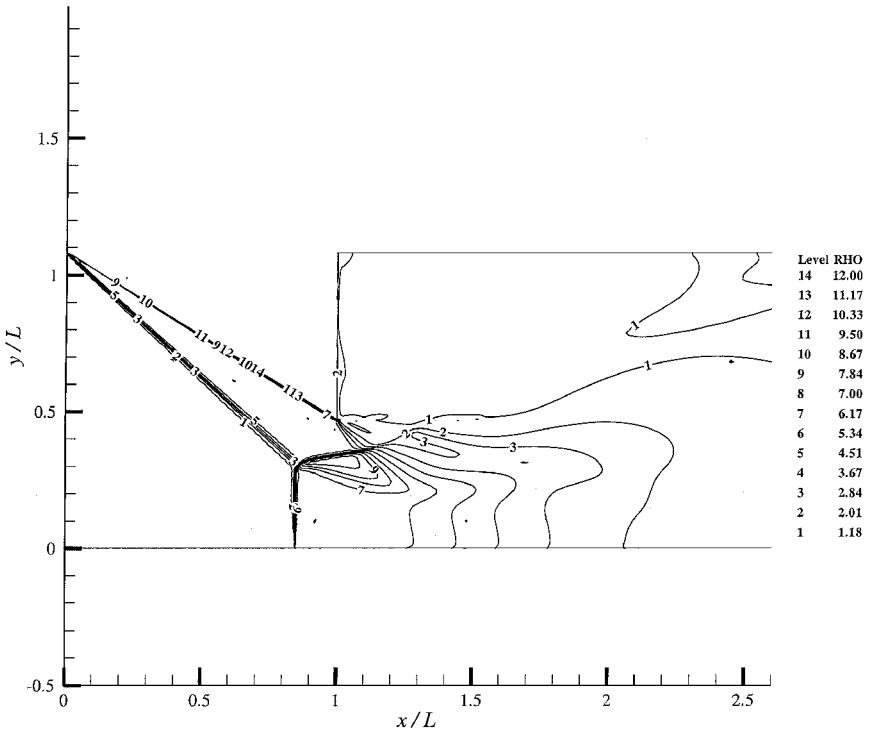

Mach reflection, θ_w = 31.5 deg

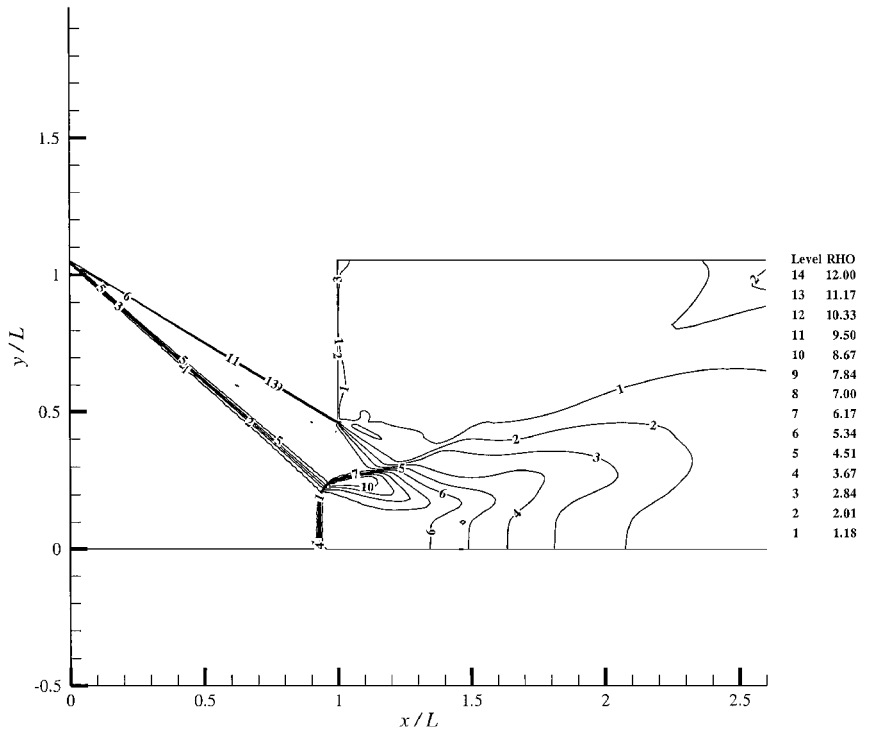

Mach reflection, θ_w = 30.5 deg

Fig. 6 Hysteresis loop at M_∞ = 7.5: iso-density contour lines (continued).

along the symmetry axis that are reported in Fig. 8 as a function of the x coordinate normalized by the size of the subsonic pocket L_s. In the figure we also report the temperature distributions obtained with the quasi-one-dimensional model.[4] The comparison indicates that the rate of thermal relaxation is affected by the multidimensionality of the flow; in particular, neglecting multidimensional effects results in a slower T-V energy transfer mechanism. In addition, the flow is also found to be chemically frozen.

With regard to the characteristic scales of the Mach stem configuration, in Figs. 9 and 10 we report, respectively, the Mach stem height H_m and the extent of the subsonic pocket L_s, and the location of the Mach stem d_m as a function of the incident shock angle.

The simulations reveal that in the investigated range of incident shock angles α_i the scales of the Mach stem configuration exhibit a nearly linear dependence upon α_i. Such a dependency is also recovered by the quasi-one-dimensional model of Ref. 4 as well as by the DSMC of Ref. 10, as Figs. 9 and 10 show. However, we must recall that the results of Ref. 10 are for wind-tunnel conditions, and they are reported here only for the sake of a qualitative comparison. The predicted Mach stem height and its location exhibit differences, with

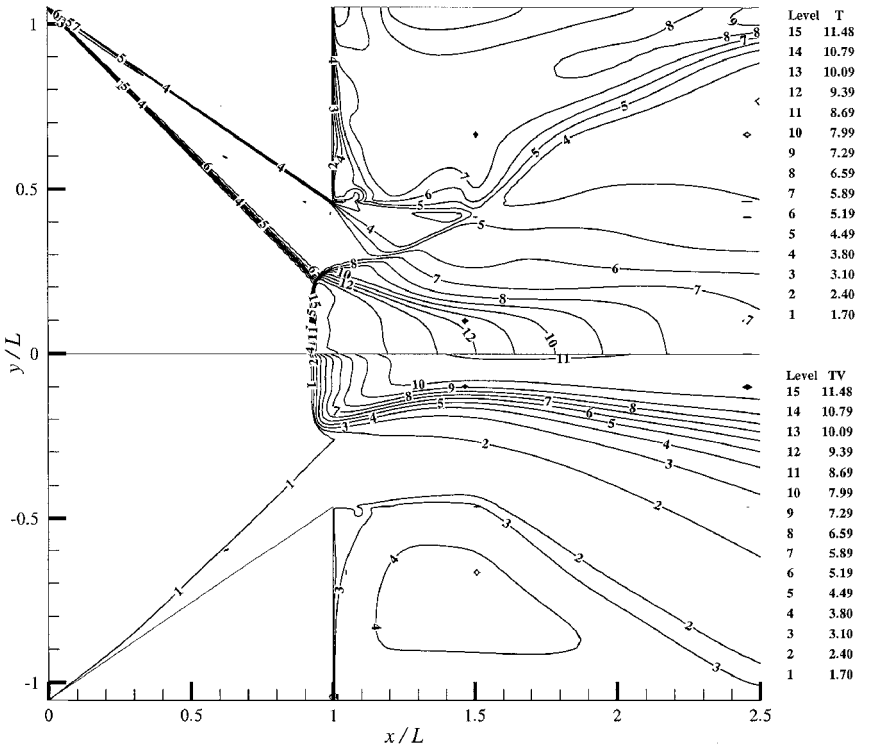

Fig. 7 Iso-temperature contour lines (M_∞ = 7.5 and θ_w = 30.5 deg): T, translational temperature, and T_V, vibrational temperature.

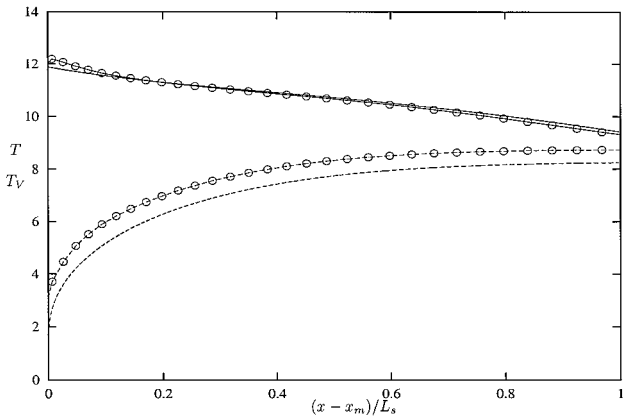

Fig. 8 Distributions of translational (——) and vibrational (– – –) temperatures along the symmetry axis (M_∞ = 7.5 and θ_w = 30.5 deg): ○, present study, and ——, quasi-one-dimensional model of Ref. 4.

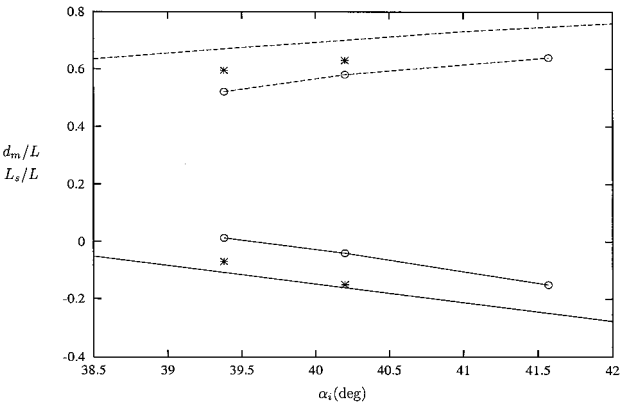

Fig. 10 Distributions of the Mach stem position (——) and subsonic pocket size (– – –) as a function of the incident shock angle at M_∞ = 7.5: ○, real gas simulation; ∗, ideal gas simulation (γ = 1.4); and ——, quasi-one-dimensional model of Ref. 4.

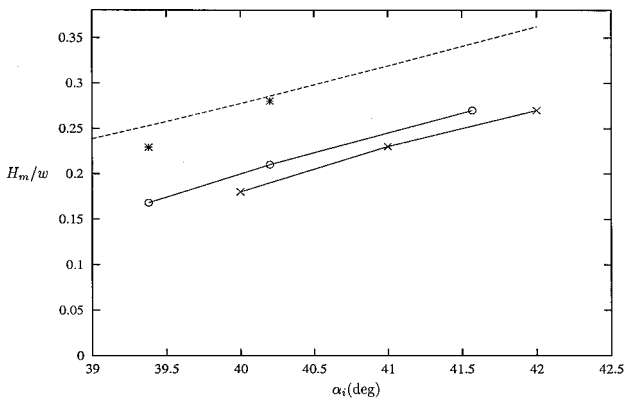

Fig. 9 Distribution of the Mach stem height as a function of the incident shock angle α_i at M_∞ = 7.5: ○, real gas simulation; ∗, ideal gas simulation (γ = 1.4); ×, DSMC simulation of Ref. 10; and – – –, quasi-one-dimensional model of Ref. 4.

respect to the quasi-one-dimensional results of Ref. 4, respectively of $\mathcal{O}$(30%) and $\mathcal{O}$(10%). For the selected freestream conditions the results show that the temperature across the stem is of $\mathcal{O}$(3000 K), whereas the peak value attained downstream of the incident and reflected shocks is of $\mathcal{O}$(1600 K). The results also show that relaxation phenomena are largely confined in the subsonic pocket. Therefore we have carried out cold flow simulations assuming a specific heat ratio γ = 1.4. The computed real and ideal gas solutions are compared in Fig. 11 in terms of the iso-pressure contour lines. The figure reveals that steady shock reflections of ideal and real gases exhibit a geometric similarity as a consequence of 1) the thermal and chemical relaxation with a feedback mechanism within the subsonic pocket and 2) the freezing of the incident and reflected shocks.[4] As already observed in Ref. 4, the real gas results show a reduction of the Mach stem and its forward displacement with respect to the ideal case; in addition, the figure also reveals a geometric scaling of the shock configuration.

Wind-Tunnel Conditions

The extrema of the hysteresis loop correspond to variations of the wedge angle in the range 35.0 deg < θ_w < 38.0 deg. The iso-density

contour lines at $\theta_w = 35$ deg reported in Fig. 12 again show the occurrence of the hysteresis. The iso-contour lines of the translational and vibrational temperatures are reported in Fig. 13, which reveals that the selected conditions lead to a fast T-V energy exchange. This is also observed in Fig. 14, where we report the distributions of translational and vibrational temperatures and nitrogen mass fraction along the symmetry axis within the subsonic pocket. With respect to thermal nonequilibrium, the figure shows the occurrence of a three-stage mechanism that controls the relaxation within the subsonic pocket. The vibrational relaxation is the controlling phenomenon on a scale of $\mathcal{O}(5–10\%)$ of the pocket size, and the flow attains vibrational equilibrium ($T = T_V$) at x_a (see Fig. 14). For $x_a < x < x_b$ we observe a T-V exchange reversal ($T < T_V$) as a consequence of the fast T-V exchange and the expansion inside the pocket with a decrease of both translational and vibrational temperatures. In particular, the difference between T and T_V first increases because of the expansion, then decreases because of a relaxation reversal that leads the flow to attain again $T = T_V$ at $x = x_b$. For $x > x_b$ the subsonic expansion is the controlling phenomenon that leads the flow to freeze at the throat where sonic conditions are attained. With regard to the

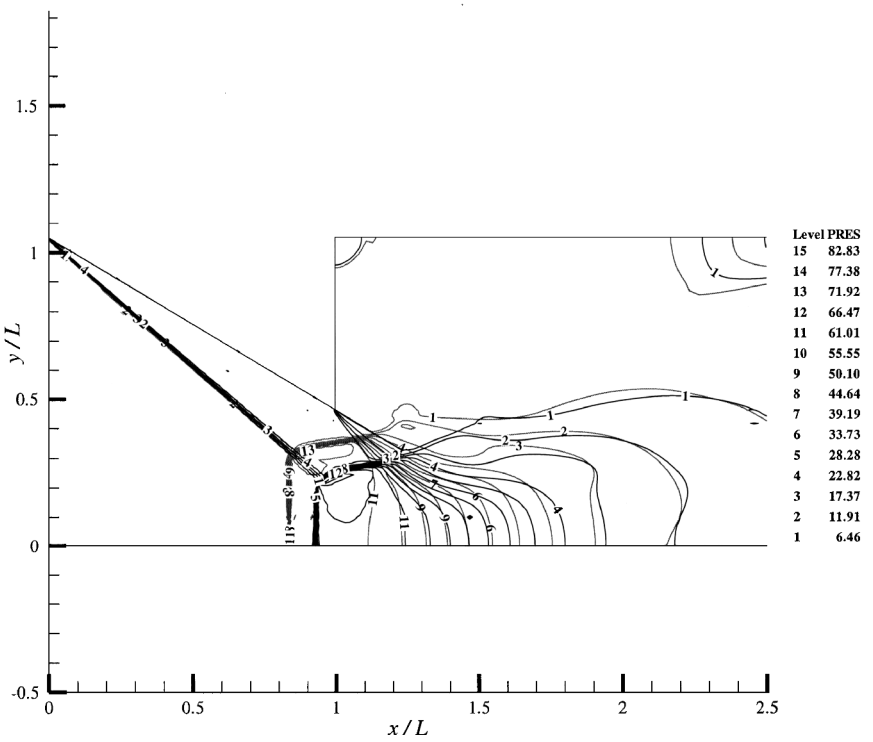

Fig. 11 Iso-pressure contour lines ($M_\infty = 7.5$ and $\theta_w = 30.5$ deg): ——, real gas simulation, and - - - -, ideal gas simulation ($\gamma = 1.4$).

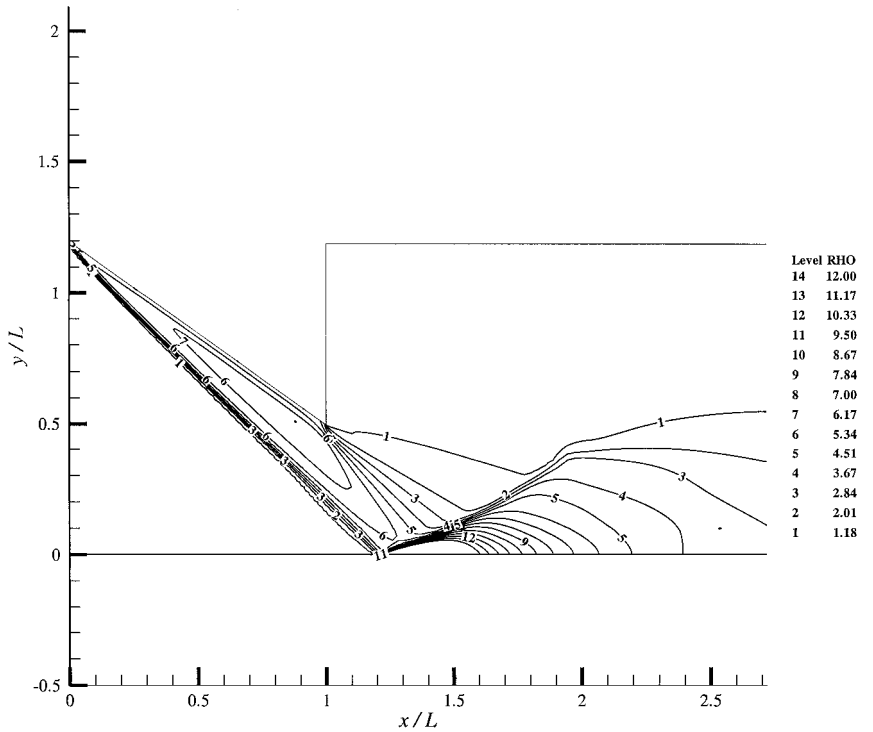

Regular reflection, $\theta_w = 35$ deg

Fig. 12 Hysteresis loop at $M_\infty = 9.8$: iso-density contour lines.

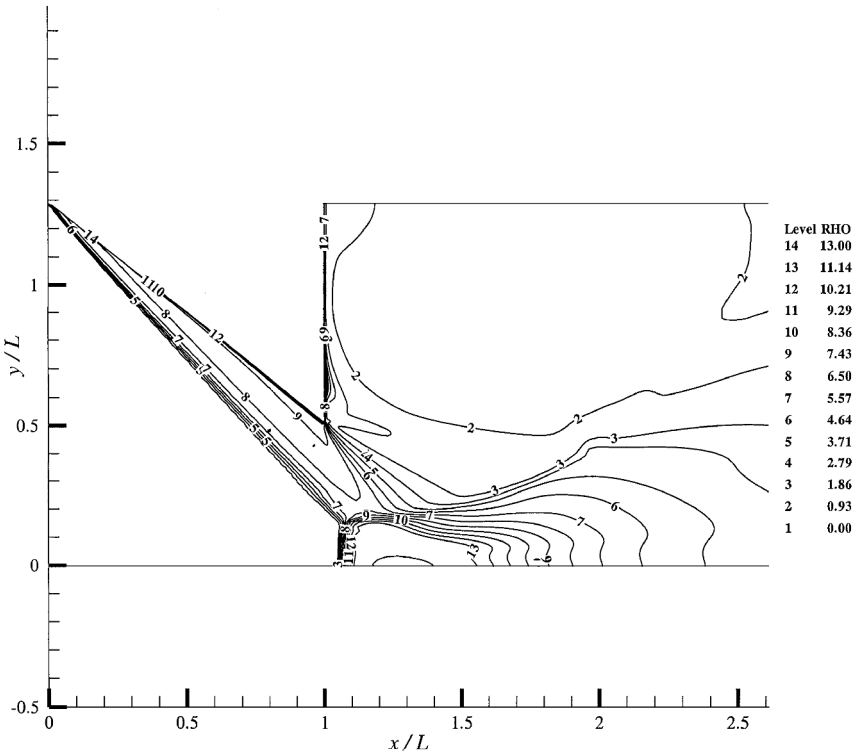

Mach reflection, θ_w = 38 deg

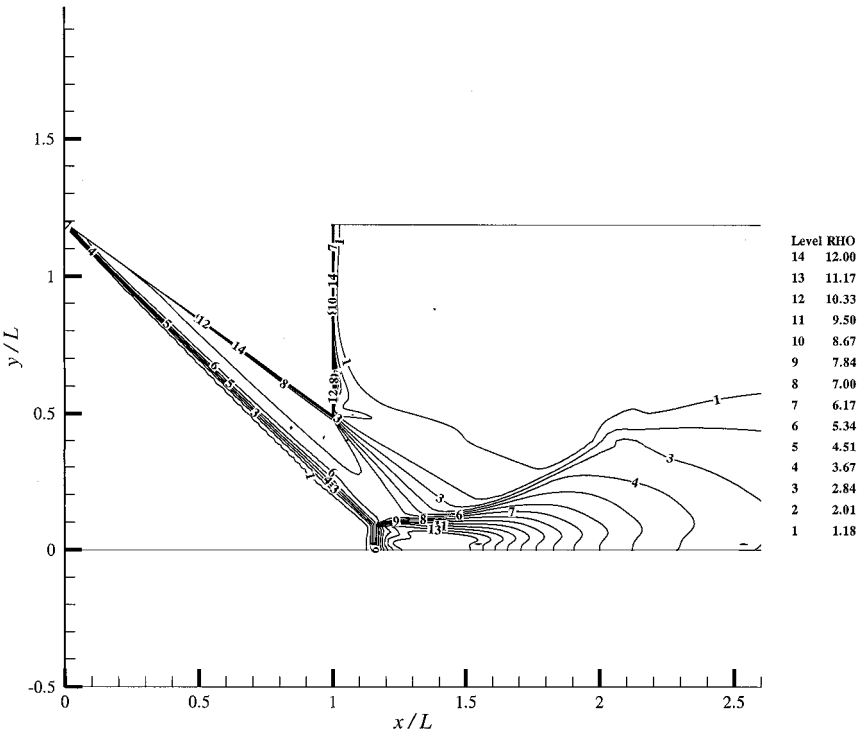

Mach reflection, θ_w = 35 deg

Fig. 12 Hysteresis loop at M_∞ = 9.8: iso-density contour lines (continued).

chemical reactions, the figure shows a two-stage evolution: the dissociation reactions are favored for $x < x_b$, whereas they are inhibited in the region where the expansion is controlling ($x > x_b$).

For the selected freestream conditions the simulations show that the shock reflection configurations also depend on relaxation phenomena taking place in regions other than the subsonic pocket (as Fig. 13 reveals). In particular, we observe that the incident shock is not straight as Fig. 15 shows, where we report the values of the computed incident shock angle as a function of the wedge angle at the leading edge of the wedge and at the triple point location. In the figure we also report the values obtained through the Rankine–Hugoniot relations for $\gamma = 1.43$ (which is the value of the specific heat ratio corresponding to the initial conditions) and $\gamma = 1.29$ (that corresponds to vibrationally fully excited conditions). The figure indicates that, at wind-tunnel conditions, relaxation phenomena affect the incident shock as well, and it suggests that the specific heat ratio attains (approximatively) the value of $\gamma = 1.29$ at the triple point. Then cold flow simulations have been carried out assuming for the specific heat ratio the value of 1.29 (for the flight-type conditions the influence of thermal relaxation on α_i is negligible, and it is not reported).

The scales of the Mach stem configuration exhibit a strong dependence upon the real gas effects, and (as in the earlier test case) the Mach stem height and its position are the most sensitive

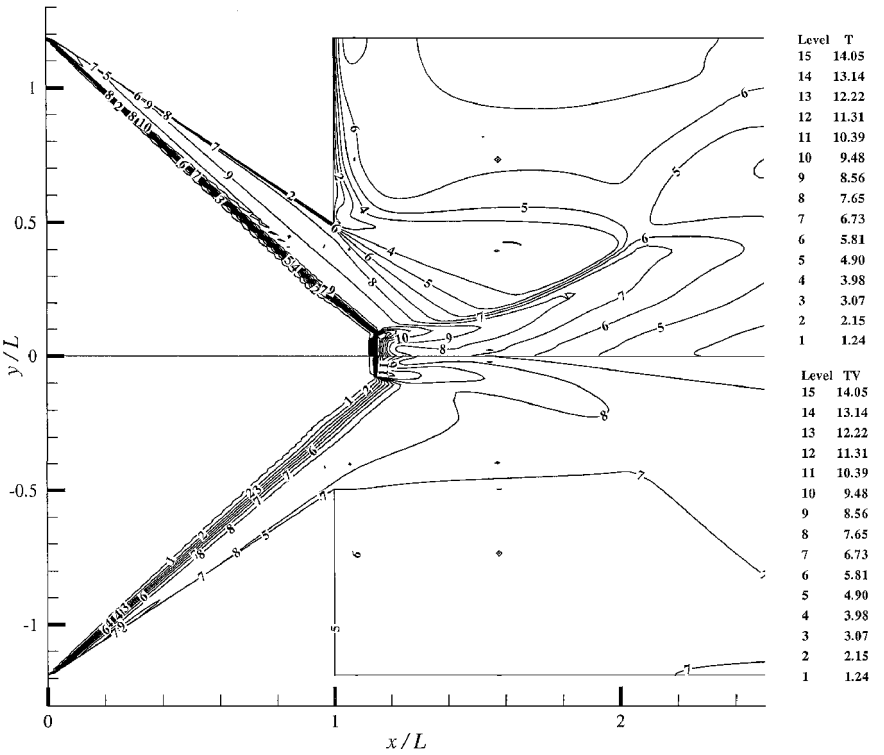

Fig. 13 Iso-temperature contour lines (M_∞ = 9.8 and θ_w = 35 deg): T, translational temperature, and T_V, vibrational temperature.

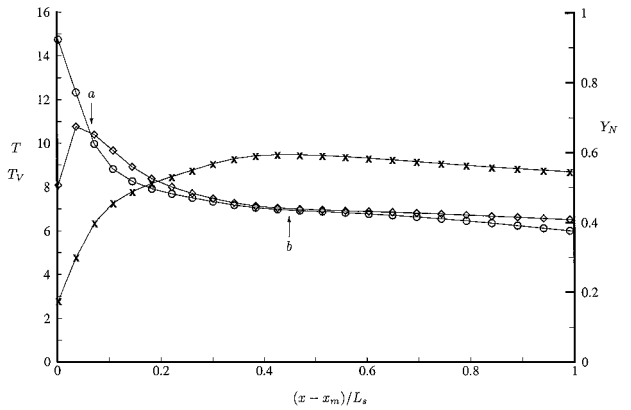

Fig. 14 Distributions of translational (○) and vibrational (◇) temperatures and atomic nitrogen mass fraction (×) along the symmetry axis (M_∞ = 9.8 and θ_w = 35 deg).

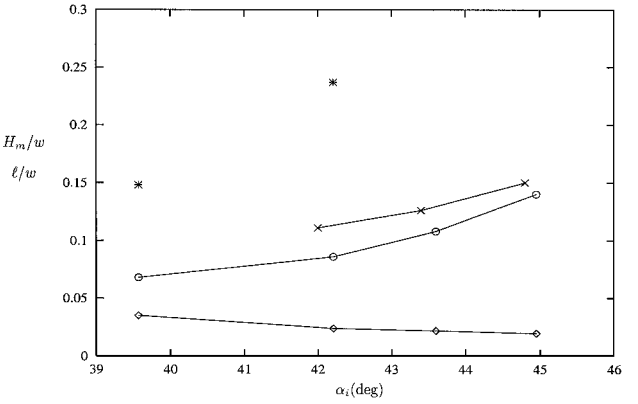

Fig. 16 Distribution of the Mach stem height H_m and the vibrational relaxation length l (normalized by the wedge length) as a function of the incident shock angle α_i at M_∞ = 9.8: ○, real gas simulation; ∗, ideal gas simulation (γ = 1.29); and ×, DSMC simulation of Ref. 10 (M_∞ = 10).

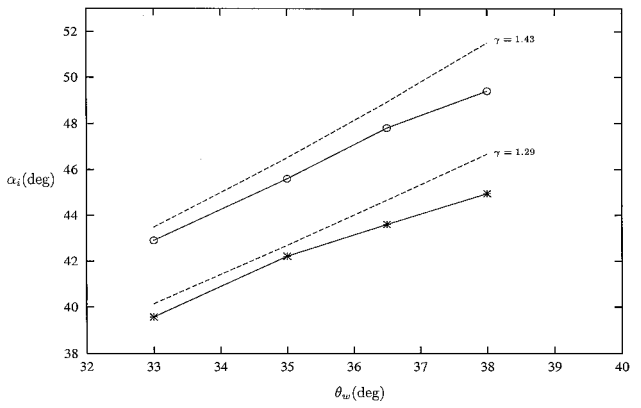

Fig. 15 Distribution of the incident shock angle α_i as a function of the wedge angle θ_w at M_∞ = 9.8 (——, computations and – – –, Rankine–Hugoniot relations): ∗, incident shock angle at triple point, and ○, incident shock angle at leading edge.

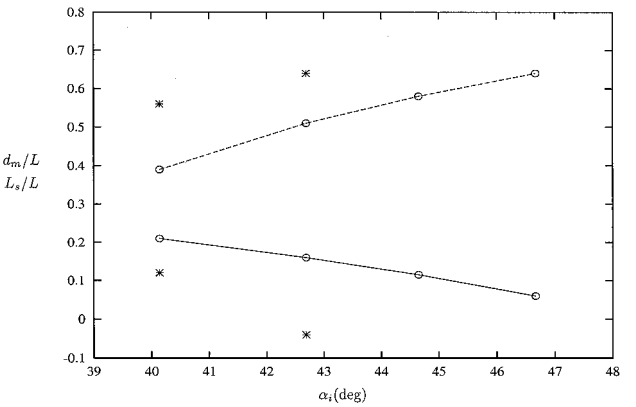

Fig. 17 Distributions of the Mach stem position (——) and subsonic pocket size (– – –) as a function of the incident shock angle at M_∞ = 9.8: ○, real gas simulation, and ∗, ideal gas simulation (γ = 1.29).

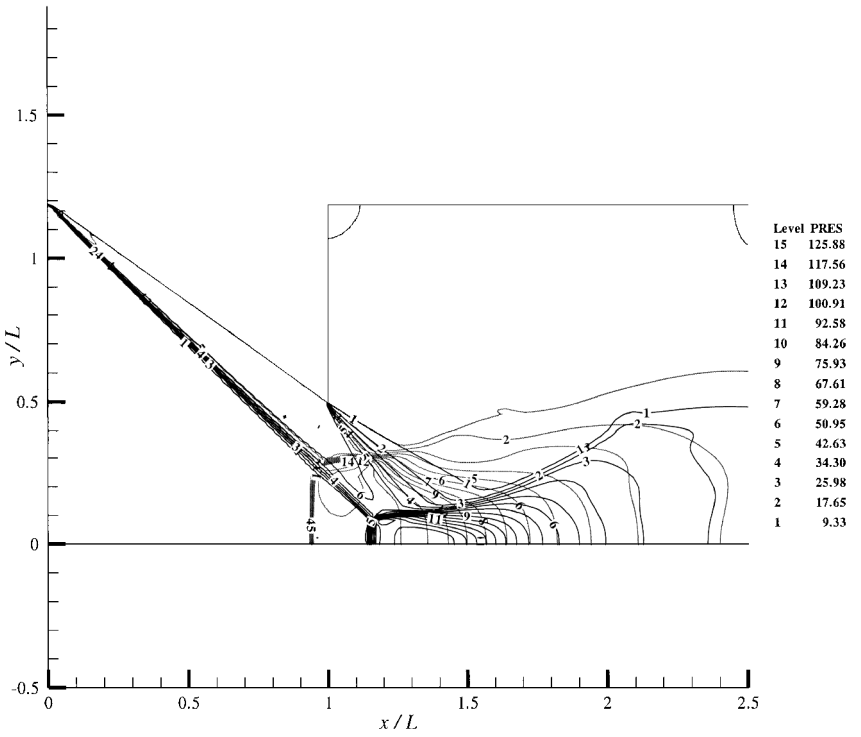

Fig. 18 Iso-pressure contour lines (M_∞ = 9.8 and θ_w = 35 deg): ——, real gas simulation, and - - - -, ideal gas simulation (γ = 1.29).

quantities to the relaxation process. Indeed, the ideal and real gas values differ by a factor of two, as shown in Figs. 16 and 17 where the distributions of H_m and d_m and L_s are reported as a function of the incident shock angle (determined at the triple point location). In addition, Fig. 16 shows that the predicted Mach stem height exhibits differences of $\mathcal{O}(10–25\%)$ with respect to the values reported in Ref. 10. We argue that the discrepancies can be caused by the uncertainties in determining the value of the incident shock angle for a given wedge angle. No comparison with the quasi-one-dimensional model of Ref. 4 is reported because the latter admits MR solutions (for the selected geometry and the given freestream conditions) only for $\theta_w \leq 35$ deg (which correspond to $\alpha_i \leq 42$ deg).

In Fig. 16 we have also reported the distribution of the relaxation length ℓ normalized by w. As one would have expected, the figure reveals that the larger the incident shock angle the larger the Mach stem height and the shorter the relaxation extent are. In addition, the figure also shows that the relaxation length attains a value that is nearly independent of the incident shock angle ($\ell \approx 0.02w$). The iso-pressure contour lines of the ideal and nonequilibrium gas simulations are reported in Fig. 18, which shows that, notwithstanding the large differences in the scales predicted with ideal and real gas assumption, cold and hot Mach stem configurations still exhibit a geometric similarity.

Conclusions

In the present paper we have studied the influence of thermal and chemical relaxation on steady shock-wave reflections by means of a two-temperature model that relies on a subdomain decomposition that exploits parallel architectures. The conditions of the study are typical of flight and wind-tunnel conditions as reported in the literature. The occurrence of the hysteresis phenomenon has been detected by rotating the wedge around the trailing edge spanning a range of shock angles between the DS and the MR regions. To quantify the effects of nonequilibrium, we have also carried out ideal gas simulations assuming different specific heat ratios for the two test conditions.

The study reveals that steady shock reflections of ideal and real gases exhibit a geometric similarity (at least for the conditions here investigated). In the presence of nonequilibrium effects, the Mach stem configurations show a scaling consisting of a reduction of the Mach stem height and its forward displacement because of the relaxation occurring downstream of the Mach stem and a feedback mechanism within the subsonic pocket. In the investigated range of incident shock angles, the Mach stem height (normalized by the wedge length w), its location, and the size of the subsonic pocket (normalized by the wedge size L) are found to scale nearly linearly with the incident shock-wave angle independently of the freestream Mach number. In addition, for low values of the freestream pressure and temperature, the simulations show that the flow is chemically frozen, and shock reflections are only affected by translation-vibration energy exchanges. At high freestream pressure and temperature shock reflections are affected both by thermal and chemical relaxation phenomena. The former is found to exhibit a three-stage evolution mechanism, whereas the latter obeys a two-stage evolution.

References

[1]Li, H., and Ben-Dor, G., "A Parametric Study of Mach Reflection in Steady Flows," *Journal of Fluid Mechanics*, Vol. 341, No. 101, 1997, pp. 101–125.

[2]Hornung, H. G., Oertel, H., and Sandeman, R. J., "Transition to Mach Reflection of Shock Waves in Steady and Pseudosteady Flow with and Without Relaxation," *Journal of Fluid Mechanics*, Vol. 90, No. 541, 1979, pp. 541–560.

[3]Gimelshein, S. F., Markelov, G. N., and Ivanov, M. S., "Real Gas Effects on the Transition Between Regular and Mach Reflections in Steady Flows," AIAA Paper 98-0877, Jan. 1998.

[4]Grasso, F., and Paoli, R., "An Analytical Study of Mach Reflection in Nonequilibrium Steady Flows," *Physics of Fluids*, Vol. 11, No. 10, 1999, pp. 3150–3167.

[5]Chpoun, A., Passerel, D., Li, H., and Ben-Dor, G., "Reconsideration of Oblique Shock Wave Reflection in Steady Flows. Part 1. Experimental Investigations," *Journal of Fluid Mechanics*, Vol. 301, No. 19, 1995, pp. 19–35.

[6]Ivanov, M. S., Gimelshein, S. F., and Beylich, A. E., "Hysteresis Effect in Stationary Reflection of Shock Waves," *Physics of Fluids*, Vol. 7, No. 4, 1995, pp. 685–687.

[7]Ivanov, M. S., Kudryavtsev, M. S., Markelov, A. N., and Gimelshein, S. F., "Transition Between Regular and Mach Reflection of Shock Waves in Steady Flows," AIAA Paper 97-2511, June 1997.

[8]Ivanov, M. S., Zeitoun, D., Vuillon, J., Gimelshein, S. F., and Markelov, G., "Investigations of the Hysteresis Phenomenon in Steady Shock Reflection Using Kinetic and Continuum Approach," *Shock Waves*, Vol. 5, No. 341, 1996, pp. 341–346.

[9]Hornung, H. G., and Robinson, M. L., "Transition from Regular to Mach Reflection of Shock Waves. Part 2. The Steady Flow Criterion," *Journal of*

Fluid Mechanics, Vol. 123, No. 155, 1982, pp. 155–164.

[10]Gimelshein, S. F., Markelov, A. N., and Ivanov, M. S., "Relaxation and Rarefaction Effects on Shock Wave Reflections," AIAA Paper 98-2819, June 1998.

[11]Burtscell, Y., and Zeitoun, D., "Transition RR→ MR in Thermochemical Nonequilibrium Flows," Twenty-Second International Symposium on Shock Waves, Paper 2250, London, July 1999.

[12]Gnoffo, P. A., Gupta, R. P., and Shinn, J. L., "Conservation Equations and Physical Models for Hypersonic Air Flows in Thermal and Chemical Nonequilibrium," NASA TP 2867, Feb. 1989.

[13]Grasso, F., and Capano, G., "Modeling of Ionizing Hypersonic Flows in Nonequilibrium," *Journal of Spacecraft and Rockets*, Vol. 32, No. 2, 1995, pp. 217–224.

[14]Park, C., *Nonequilibrium Hypersonic Aerothermodynamics*, Wiley, New York, 1992, pp. 255–328.

[15]Quarteroni, A., "Domain Decomposition Methods for Systems of Conservation Laws: Spectral Collocation Approximation," Inst. for Computer Applications in Science and Engineering, Rept. 89-5, Hampton, VA, May 1989.

[16]Liu, Y., and Vinokur, M., "Upwind Algorithms for General Thermochemical Nonequilibrium Flows," AIAA Paper 89-0201, Jan. 1989.

[17]Roe, P. L., "Approximate Riemann Solvers, Parameters Vectors, and Difference Schemes," *Journal of Computational Physics*, Vol. 43, No. 2, 1981, pp. 357–372.

I. D. Boyd
Associate Editor